

Crystal Structures and Rotational Dynamics of a Two-dimensional Metal Halide Perovskite (OA)₂PbI₄

Xiao Hu^{1,*}, Depei Zhang¹, Tianran Chen¹⁺, Alexander Z. Chen², Eric N. Holmgren², Qiang Zhang³, Daniel M. Pajerowski³, Mina Yoon⁴, Guangyong Xu⁵, Joshua J. Choi² and Seung-Hun Lee^{1,*}

¹ Department of Physics, University of Virginia, Charlottesville, Virginia 22904, USA.

² Department of Chemical Engineering, University of Virginia, Charlottesville, Virginia 22904, USA.

³ Neutron Scattering Division, Oak Ridge National Laboratory, Oak Ridge, Tennessee 37831, USA.

⁴ Center for Nanophase Materials Sciences, Oak Ridge National Laboratory, Oak Ridge, Tennessee 37831, USA.

⁵ NIST Center for Neutron Research, National Institute of Standards and Technology, Gaithersburg, Maryland 20899, USA.

+ Now at the NIST Center for Neutron Research, National Institute of Standards and Technology, Gaithersburg, Maryland 20899, USA.

* Corresponding Authors. Emails: xh5fe@virginia.edu and shlee@virginia.edu

This manuscript has been authored by UT-Battelle, LLC, under contract DE-AC05-00OR22725 with the US Department of Energy (DOE). The US government retains and the publisher, by accepting the article for publication, acknowledges that the US government retains a nonexclusive, paid-up, irrevocable, worldwide license to publish or reproduce the published form of this manuscript, or allow others to do so, for US government purposes. DOE will provide public access to these results of federally sponsored research in accordance with the DOE Public Access Plan (<http://energy.gov/downloads/doe-public-access-plan>).

ABSTRACT

The extended charge carrier lifetime in metal halide perovskites is responsible for their excellent optoelectronic properties. Recent studies indicate that the superb device performance in these materials is intimately related to the organic cation dynamics. Here, we focus on the investigation of the two-dimensional hybrid perovskite, $(\text{C}_8\text{H}_{17}\text{NH}_3)_2\text{PbI}_4$ (henceforth $\text{OA}^+ = \text{C}_8\text{H}_{17}\text{NH}_3^+$). Using elastic and quasi-elastic neutron scattering techniques and group theoretical analysis, we studied the structural phase transitions and rotational modes of the $\text{C}_8\text{H}_{17}\text{NH}_3^+$ cation in $(\text{OA})_2\text{PbI}_4$. Our results show that, in the high-temperature orthorhombic ($T > 310$ K) phase, the OA^+ cation exhibits a combination of a two-fold rotation of the $\text{NH}_3 - \text{CH}_2$ head group about the crystal $c - \text{axis}$ (C_2) with a characteristic relaxation time of ~ 6.2 picoseconds, three-fold rotations (C_3) of NH_3 and CH_3 terminal groups and slow librations of the other atoms. Contrastingly, only the C_3 rotation is present in the intermediate-temperature orthorhombic ($238 \text{ K} < T < 310 \text{ K}$) and low-temperature monoclinic ($T < 238 \text{ K}$) phases.

INTRODUCTION

Metal halide perovskites (MHPs), such as $\text{CH}_3\text{NH}_3\text{PbI}_3$, have been intensively studied in recent years for their attractive electronic, optical and optoelectronic properties. The high device performances of MHPs result from their unique properties such as changeable bandgap, extended charge carrier lifetime, and high light absorption¹⁻¹¹. Some microscopic mechanisms have been reported to account for these special properties, such as polaronic features dominant in three-dimensional (3D) MHPs with organic molecules^{6, 12-23}, excitonic features dominant in MHPs with

lower dimensionality such as two-dimensional (2D) MHPs^{24, 25}, and coexistence in other cases²⁶⁻²⁸. Recent investigations^{21-22, 29-32} and our previous studies have illuminated the role of organic molecules in the phonon melting and charge screening in 3D MHPs^{6, 33}.

In this work, we investigate the structural phase transitions and rotational dynamics of organic cations in the two-dimensional hybrid perovskite, octyl-ammonium lead iodide³⁴ ((OA)₂PbI₄, where OA⁺=C₈H₁₇NH₃⁺), by performing neutron diffraction measurements and quasi-elastic neutron scattering as a function of temperature, 100 K < *T* < 370 K, covering the three different structural phases of (OA)₂PbI₄. Our quasi-elastic neutron data enabled us to apply a group theoretical analysis based on the crystal structure to understand the nature of the rotation motion of the OA⁺ cation, and the resulting model includes the symmetry and relaxation times as a function of temperature. Our analysis shows that, in the high temperature (HT) phase (*T* > 310 K), the OA⁺ cation presents a combination of a two-fold rotation (C₂) of the head group NH₃ – CH₂, around the crystallographic *c*-axis, three-fold rotations (C₃) of terminal CH₃ and NH₃ groups, and slow librations of the remaining CH₂ groups. While in the intermediate temperature (IT) and low temperature (LT) phases, only the C₃ rotations exist. Upon further cooling in the LT phase (*T* < 170 K), the C₃ rotation is difficult to detect within the instrument resolution. On the other hand, our diffraction data show that upon heating

the thermal factor associated with atomic thermal fluctuations increases dramatically as the system enters the IT phase.

RESULTS

Phase transitions and crystal structures of $(\text{OA})_2\text{PbI}_4$. To study the structural phase transitions of $(\text{OA})_2\text{PbI}_4$, we performed elastic neutron scattering on a $\sim 5\text{g}$ non-deuterated $(\text{OA})_2\text{PbI}_4$ powder sample as a function of temperature, at the Spin Polarized Inelastic Neutron Spectrometer (SPINS, NG-5) located at the NCNR. Manifested by the peak appearance or disappearance, Figure 1A shows that the system undergoes two structural phase transitions upon cooling, at $210(5)\text{ K}$ and $305(5)\text{ K}$. Upon heating, however, the transitions occur at $245(5)\text{ K}$ and $310(5)\text{ K}$, as shown in Fig. 1B. This thermal hysteresis, which is also reported in the differential scanning calorimetry (DSC) experiment (Fig. S1), indicates that there are energy barriers between the structural phases.

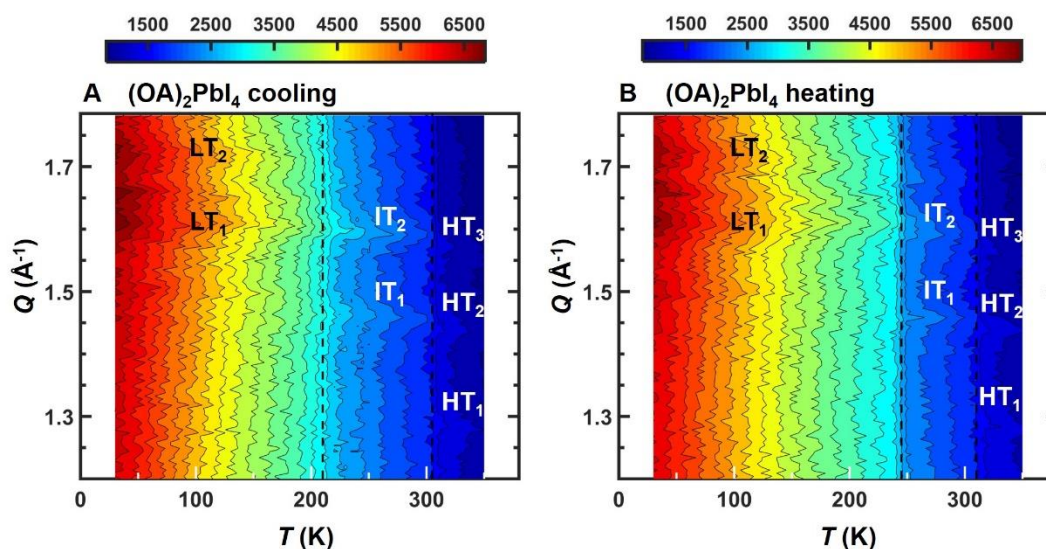


Fig. 1 Structural transitions of $(\text{OA})_2\text{PbI}_4$. Elastic neutron scattering data obtained

at SPINS, NCNR, (A) for cooling and (B) for heating process. (A) and (B) are contour maps of the scattering intensity as a function of momentum transfer, Q , and temperature, T . Q range of 1.200 \AA^{-1} to 1.785 \AA^{-1} was covered. Some merged Bragg peaks with dominant intensities in each phase are indexed as: HT₁, HT₂, HT₃, IT₁, IT₂, LT₁, LT₂.

In order to refine the crystal structures of the three different phases, we have performed neutron diffraction measurements on a ~1g deuterated powder sample of (OA)₂PbI₄ using the powder diffractometer (POWGEN, BL-11A) at the Oak Ridge National Laboratory (ORNL) located in Oak Ridge, Tennessee, USA. Figure 2 shows the neutron diffraction data obtained in the three different phases. As shown in Fig. 2A, at 350 K in the high temperature (HT) phase, the data can be reproduced by the orthorhombic structure with *Acam* symmetry and lattice constants of $a_H = 8.7615 \text{ \AA}$, $b_H = 8.7634 \text{ \AA}$, $c_H = 41.0560 \text{ \AA}$. The overlaid images on Fig. 2 show the refined structural configuration in which the long-chain molecule is curled beyond the edge of the PbI₃ sublattice. The bending of the molecule greatly suppresses its possible rotation modes in the HT phase. In principle, the whole-molecular rotation of the OA⁺ cation is forbidden due to this configuration, during which the OA⁺ cation would collide with adjacent OA⁺ cations.

Figure 2B shows the diffraction data obtained at 270 K in the intermediate temperature (IT) phase. Additional Bragg peaks that cannot be indexed by the HT *Acam* symmetry appear, such as the orthorhombic

(102). These additional peaks can be indexed by an orthorhombic structure with the $Pbca$ space group and lattice constants of $a_I = 8.9660 \text{ \AA}$, $b_I = 8.6873 \text{ \AA}$, $c_I = 37.5264 \text{ \AA}$. The bending cation reshapes into a straight chain oriented along the c -axis of the unit cell, as shown in Fig. 2B. Upon further cooling into the low temperature (LT) phase, the diffraction data show the appearance of even more peaks, such as a monoclinic (011) shown in Fig. 2C, indicating the further reduction in symmetry. The LT phase Bragg peaks can be indexed by the monoclinic structure with $P2_1/a$ space group and lattice constants of $a_L = 8.4289 \text{ \AA}$, $b_L = 8.9497 \text{ \AA}$, $c_L = 18.5813 \text{ \AA}$ and $\beta = 96.0328^\circ$. Detailed structural parameters for all three phases are listed in the supplementary information.

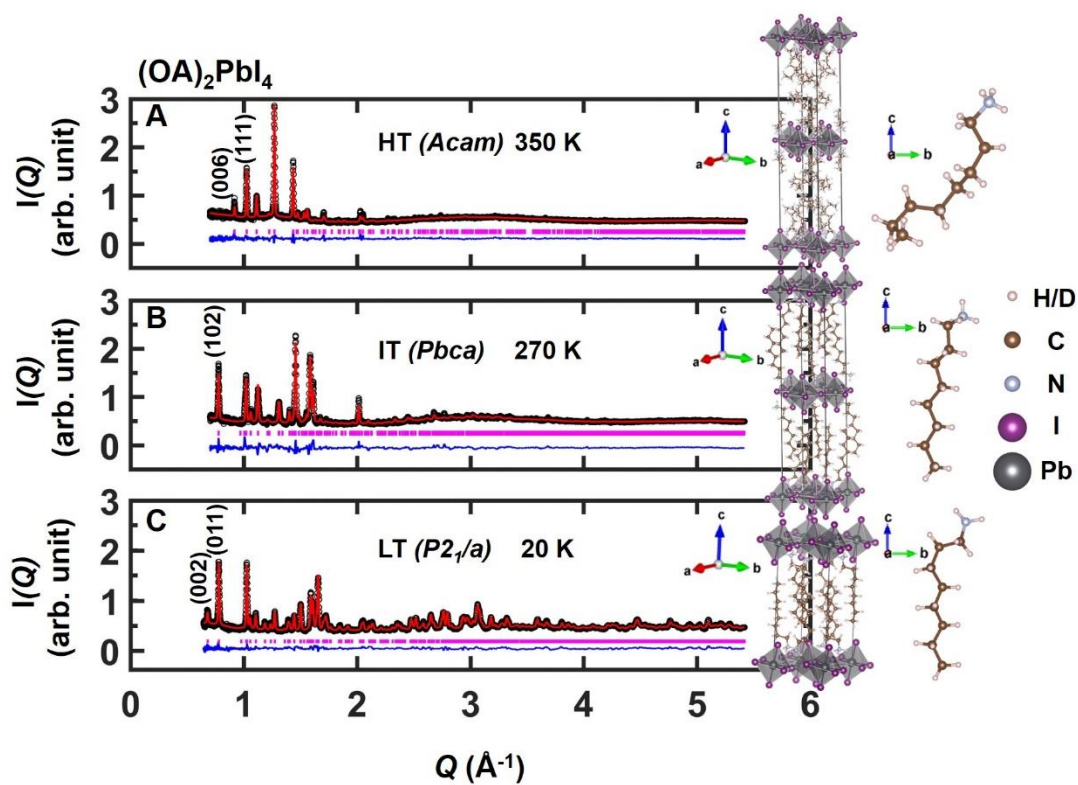


Fig. 2 Neutron diffraction patterns of deuterated (OA)₂PbI₄. Measured at (A) 350 K, (B) 270 K, and (C) 20 K. The neutron intensities are plotted in arbitrary units (arb. units). Refined structures and cation configurations are plotted as the insets. The spheres in dark gray, violet, light blue, brown and pink represent Pb, I, N, C and H/D atoms, respectively.

Note that the diffraction pattern at 20 K has sharp Bragg peaks at high Q s while at 270 K and 350 K those high Q Bragg peaks become very weak. This indicates that at 270 K and 350 K the atoms thermally fluctuate very severely from their equilibrium positions. Fig. 3 shows the average refined isotropic thermal factors U_{iso} associated with the thermal fluctuations of each type of atom are plotted as a function of temperature with the error bar describing the standard deviations. At low temperature, the ions are tightly bounded through the Coulomb interactions due to the ionic character of this crystal. When the temperature increases, thermodynamics plays a more important role and loosens the ionic bonds. As the temperature increases, the ions vibrate around more to yield large U_{iso} values (Fig. 3), which is proportional to the root-mean-square atomic displacements from their equilibrium positions.

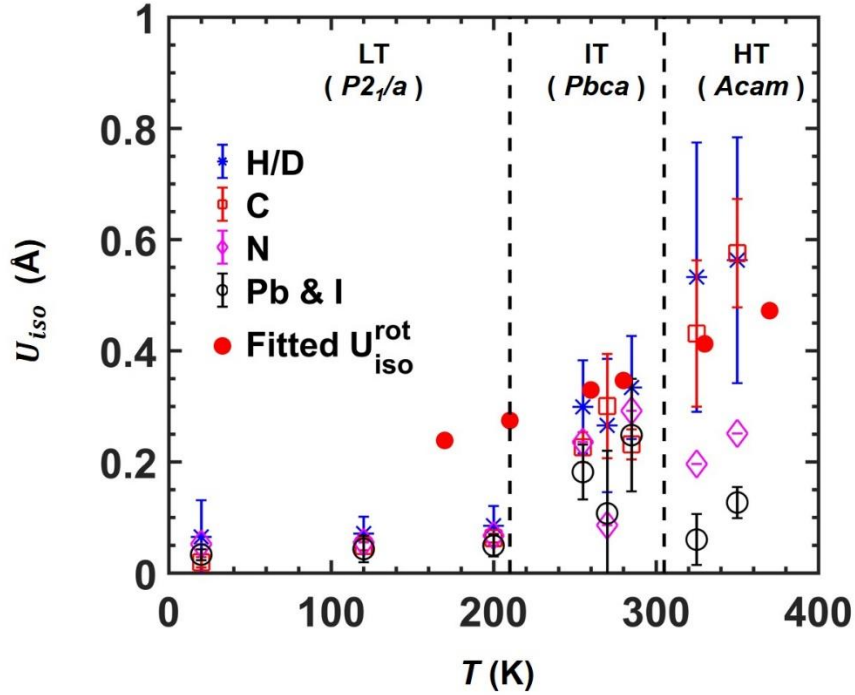


Fig. 3 Temperature dependence of thermal factors U_{iso} . Diffraction patterns at 8 different temperatures upon cooling have been refined and corresponding the isotropic thermal factor U_{iso} of different atoms are plotted. The values are the average U_{iso} of each type of atom with standard deviations: deuterium (blue star), carbon (red square), nitrogen (pink diamond), lead and iodine (black circle). The fitted thermal factor U_{iso}^{rot} in the rotation model is also plotted (red dots).

To understand the mechanism of the two structural transitions, we identify one possible transition pathway for each transition and performed first-principles density functional theory (DFT) calculations on the structures with constrained optimization to estimate the configurations and energies along the pathway. Figure 4A shows some of the intermediate structures along the transition pathway from the LT phase to the IT phase. This pathway involves an in-plane shift of the inorganic layers in the a -direction of the LT phase along with a torsion in the head

group $\text{NH}_3 - \text{CH}_2$ of the organic molecule. The black and red lines illustrate the deformation of the crystallographic unit cell. The LT and IT states are separated by an energy barrier with an order of hundreds of milli-electron volts in height, as shown in Figure 4B. With the temperature increasing, the increase in isotropic thermal factor at the LT-to-IT structural transition, shown in Fig. 3, indicates that the LT – IT transition could be driven by the increase of the entropy term associated with the atomic thermal fluctuations, such as the jiggling of the Pb – I octahedron, in the Helmholtz free energy.

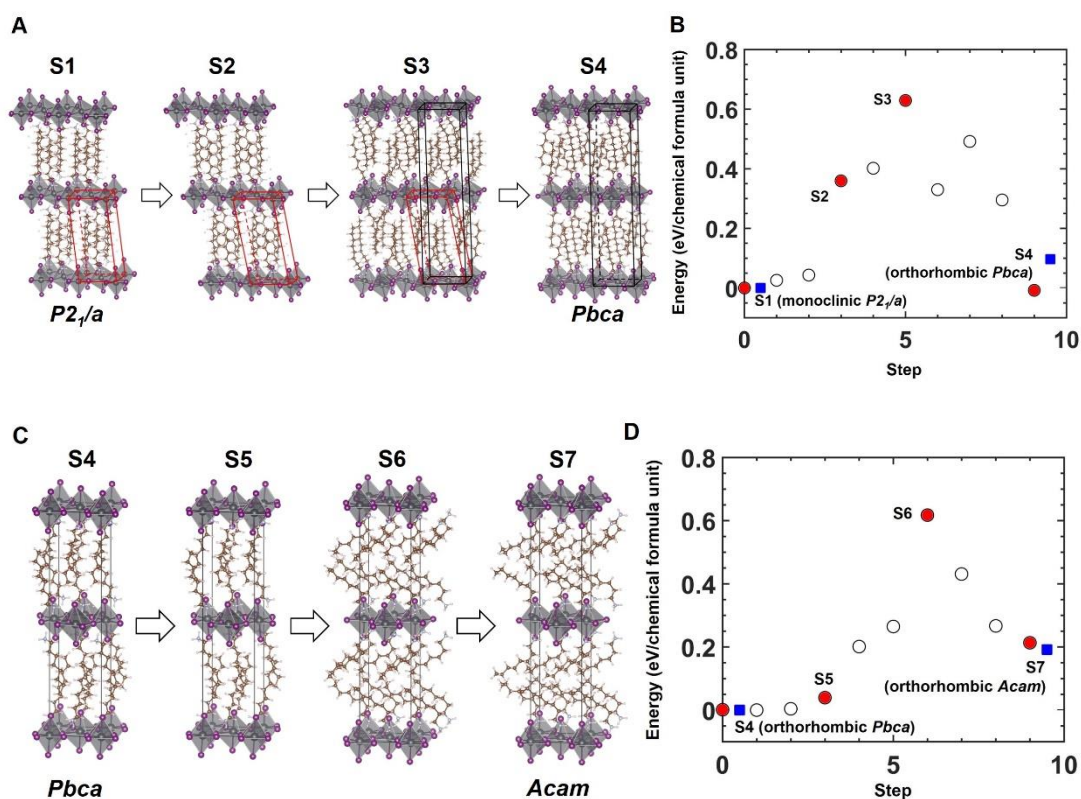


Fig. 4 Transition pathway and energy barrier. (A) Illustration of a possible pathway from the monoclinic (LT phase) to the orthorhombic (IT phase) structure. The black and red lines were drawn to show the estimated deformation of the crystal unit

cells. (B) Calculated relative energies of the constrained optimized structures without the Van der Waals correction along the pathway. (C) Illustration of a possible pathway from orthorhombic IT structure to the orthorhombic HT structure. (D) Calculated relative energies of the constrained relaxed structures without the Van der Waals correction along the pathway. Blue squares in panel (B) and (D) are the calculated relative energies with the Van der Waals interaction for the equilibrium states in LT, IT and HT phases.

The transition pathway from IT phase to HT phase is identified by a lattice elongation in the c -direction and a slight contraction in the ab plane, along with a bending of the organic cation away from c -axis across the center of the inorganic lattice. Some of the possible intermediate structures are shown in Figure 4C with the calculated system energies (Fig. 4D). It is a puzzle how the organic cation bends dramatically in the HT phase ($T > 310$ K), when compared to the IT and LT phases below 310 K. We will show below that the HT phase has very different rotational dynamics than in the IT and LT phases, which might be the reason for the bending of the organic cation only in the HT phase.

Quasi-elastic scattering from $(\text{OA})_2\text{PbI}_4$. In order to evaluate the rotational dynamics of the OA cation, we performed quasi-elastic neutron scattering on a powder sample of non-deuterated $(\text{OA})_2\text{PbI}_4$, using the Cold Neutron Chopper Spectrometer (CNCS) at ORNL. Figure 5 shows 3D quasi-elastic scattering data from $(\text{OA})_2\text{PbI}_4$, measured at six different

temperatures with CNCS upon cooling.

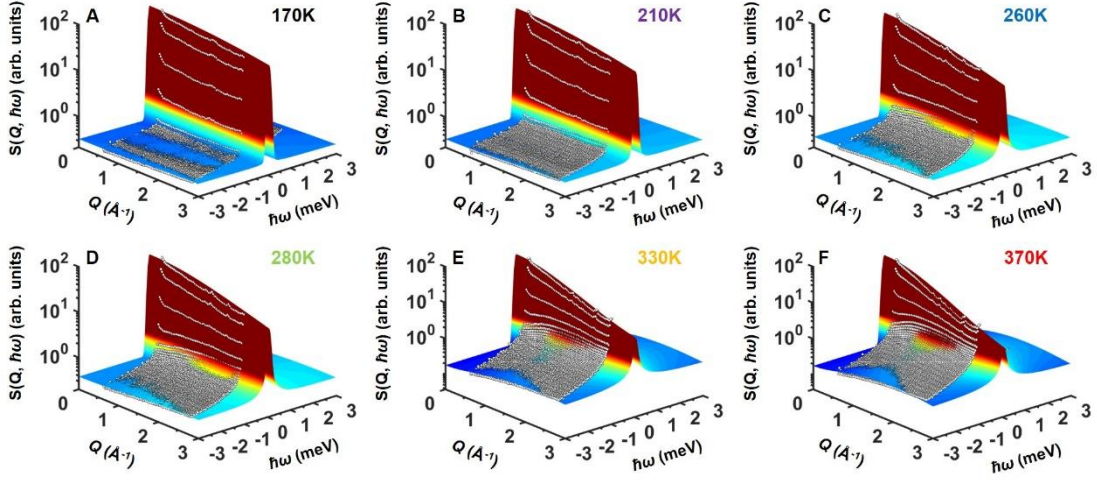


Fig. 5 Quasi-elastic scattering from OA2PbI4. Neutron scattering intensity is shown as a function of momentum (Q) and sample energy ($\hbar\omega$) transfers, measured (A) at 170K, (B) at 210K, (C) at 260K, (D) at 280K, (E) at 330K, and (F) at 370K. The data were taken using a Cold Neutron Chopper Spectrometer, CNCS. White circles are the data, and the color-coded surface is the surface image of the model calculated quasi-elastic intensity described in the text.

At 370 K in the high-temperature (HT) orthorhombic phase, there is a broad peak centered at $\hbar\omega = 0$ meV. Upon cooling into the intermediate-temperature (IT) orthorhombic phase, as shown at 280K, this elastic peak becomes narrower in energy. Upon further cooling to 210K in the low-temperature (LT) monoclinic phase, the quasi-elastic signal moves to even lower energies and becomes unresolved from the elastic signal due to the instrumental energy resolution of 0.1 meV. We chose to do fittings in the negative-energy region because it is free from phonon effects at low temperatures and has less noise than the

positive-energy region at high temperatures.

To better visualize the quasi-elastic and elastic signals, we integrated the data over three different energy windows, $-0.1 < \hbar\omega < 0.1$ meV, $-0.4 < \hbar\omega < -0.2$ meV, and $-1.0 < \hbar\omega < -0.8$ meV and plotted their Q -dependence, $S(Q)$.

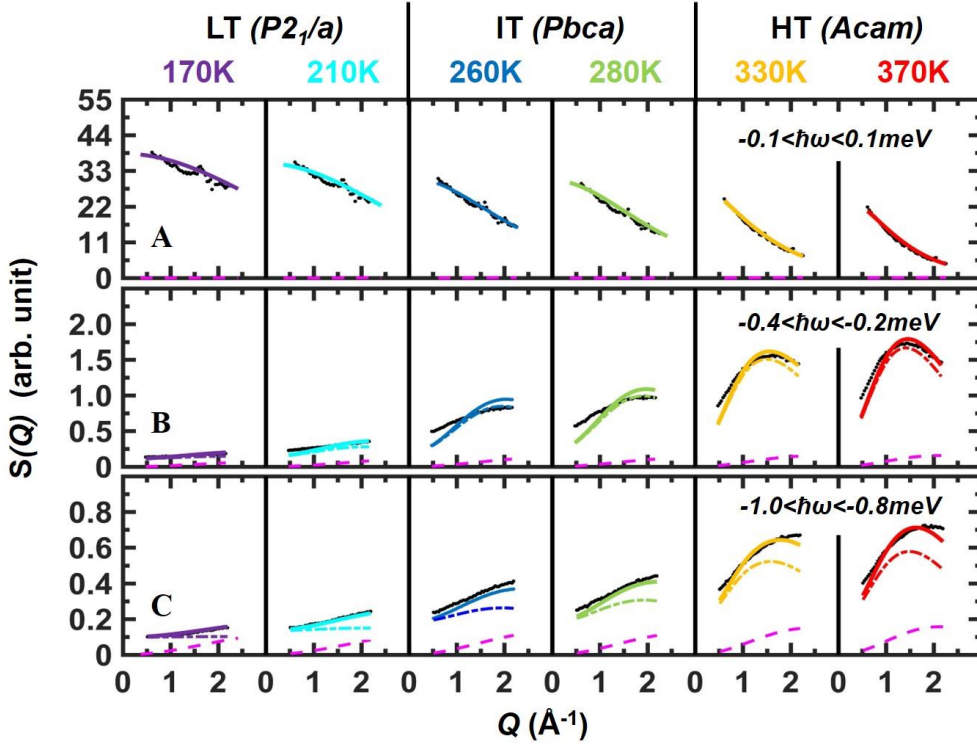


Fig. 6 Constant energy cuts of the $(\text{OA})_2\text{PbI}_4$ neutron scattering data. - Q -dependence of the neutron scattering intensity of three different energy regions of (A) $-0.1 < \hbar\omega < 0.1$ meV (slight modification is performed during the integration to balance the influence from positive-energy data), (B) $-0.4 < \hbar\omega < -0.2$ meV, and (C) $-1.0 < \hbar\omega < -0.8$ meV are plotted for six different temperatures. Black dots are the energy-integrated data, and the solid colored lines are the jump model fittings. The pink dash lines are phonon contributions and colored dash lines are rotation contributions. The lines are color-coded according to temperature: 170K(purple), 210K(cyan), 260K(blue), 280K(green) and 330K(orange) and 370K(red).

In the energy range $-0.1 < \hbar\omega < 0.1$ meV (Fig. 6A), at each temperature, the intensity decreases with increasing Q due to the Debye-Waller factor. As the temperature decreases, the elastic intensity becomes higher while the quasi-elastic intensity goes lower due to the inhibition of the rotational motion of the organic cation.

For the $-0.4 < \hbar\omega < -0.2$ meV energy window (Fig. 6 B), at 370 K, $S(Q)$ is peaked at $Q \sim 1.5 \text{ \AA}^{-1}$. Upon cooling down to 260 K, the intensity peak gradually shifts to higher $Q \sim 2.0 \text{ \AA}^{-1}$ and the magnitude greatly decreases. Upon further cooling, more prominent changes occur; at 210 K and 170 K, the intensity peak is not observed. $S(Q)$ becomes much weaker for $-1.0 < \hbar\omega < -0.8$ meV (Fig. 6 C). The weak intensity at 170 K over these energy windows is consistent with the strong enhancement of the intensity in the energy window $-0.1 < \hbar\omega < 0.1$ meV (Fig. 6 A).

Introduction to jump models^{33, 35}

Because of the strong incoherent neutron scattering amplitude of hydrogen atoms, neutron scattering measurements provide a superb sensitivity toward probing dynamics of the OA^+ cation. By analyzing the Q and $\hbar\omega$ dependent scattering intensity, the nature of hydrogen motion can be determined.

The rotation model that accounts for the preferential molecular orientation is called jump model. The rotational motion of the OA^+ cation is restricted by its own symmetry as well as the local crystal symmetry. In principle, it is almost impossible for the long OA^+ to obtain an isotropic rotation due to limitations based on its size, shape and local energy landscape. Here we only consider proper rotations instead of improper rotations such as inversion and mirror reflections. Group theory has been discussed thoroughly and we simply repeat the basic formalism as following. The scattering function for rotational motions of molecules in a crystal can be written as ^{33, 35}

$$S(Q, \hbar\omega) = e^{-\langle u^2 \rangle Q^2} \left(\sum_{\gamma} A_{\gamma}(Q) \frac{1}{\pi} \frac{\omega_{\gamma}}{1 + \omega^2 \tau_{\gamma}^2} \right) \quad (1)$$

Where $e^{-\langle u^2 \rangle Q^2}$ is the Debye Waller factor, $\langle u^2 \rangle$ is the mean squared atomic displacement, and the sum over γ runs over all the irreducible representations Γ_{γ} of Γ . The structure factor $A_{\gamma}(Q)$ is given by ^{33, 35}

$$A_{\gamma}(Q) = \frac{l_{\gamma}}{g} \sum_{\alpha} \sum_{\beta} \chi_{\gamma}^{\alpha\beta} \sum_{C_{\alpha}} \sum_{M_{\beta}} j_0(Q|\mathbf{R} - C_{\alpha}M_{\beta}\mathbf{R}|) \quad (2)$$

Where g is the order of group Γ and l_{γ} is the dimensionality of Γ_{γ} . The sums $\sum_{\alpha} \dots$ and $\sum_{\beta} \dots$ run over all the classes of C and M , respectively. The sums over $\sum_{C_{\alpha}} \dots$ and $\sum_{M_{\beta}} \dots$ run over all the rotation operations belonging to the crystal class, α , and to the molecule class, β , respectively. The characters of Γ_{γ} , $\chi_{\gamma}^{\alpha\beta}$, are the products of the characters of $C_{\gamma C}$ and $M_{\gamma M}$, $\chi_{\gamma}^{\alpha\beta} = \chi_{\gamma C}^{\alpha} \chi_{\gamma M}^{\beta}$. Here, $j_0(x)$ is the zeroth

spherical Bessel function and, $|\mathbf{R} - C_\alpha M_\beta \mathbf{R}|$, represents the distance between the initial atom position \mathbf{R} and final atom position $C_\alpha M_\beta \mathbf{R}$, called the jump distance. The relaxation time for the Γ_γ mode, τ_γ , is calculated as^{33, 35}

$$\frac{1}{\tau_\gamma} = \sum_{\alpha} \frac{n_{\alpha}}{\tau_{\alpha}} \left(1 - \frac{\chi_{\gamma}^{\alpha e}}{\chi_{\gamma}^{Ee}} \right) + \sum_{\beta} \frac{n_{\beta}}{\tau_{\beta}} \left(1 - \frac{\chi_{\gamma}^{E\beta}}{\chi_{\gamma}^{Ee}} \right) \quad (3)$$

where n_{α} , n_{β} are the number of symmetry rotations of the classes, α and β , respectively. E and e represent the identity operations of C and M .

Here we provide the simplest jump models that reproduce our CNCS data. For the HT phase, we divided the cation rotation into three parts:

(1) NH_3 - CH_2 rotation:

For one head part of the cation, two modes are expected: C_2 rotation of the NH_3 - CH_2 group around the c -axis across the center of the inorganic cage, and C_3 rotation of NH_3 head group, as shown in Fig. 7 A and B.

(2) CH_3 rotation:

For the other end of the cation, CH_3 , we used $\Gamma = C_3$ where C_3 represents the three-fold symmetry of the CH_3 group, as shown in Fig. 7 C.

(3) Librations of other CH_2 :

Theoretically, other CH_2 groups would not stay static during the complex rotation motion of the cation. Thus, we introduce a libration

model to simulate the behavior of other CH₂ groups on average (Fig. 7 A). During the slow libration, the cation body consisting of six CH₂ groups will deform accordingly.

According to a recent X-ray diffraction study³⁴ and our neutron diffraction data, the long-chain OA⁺ cation lies along *c*-axis and bends

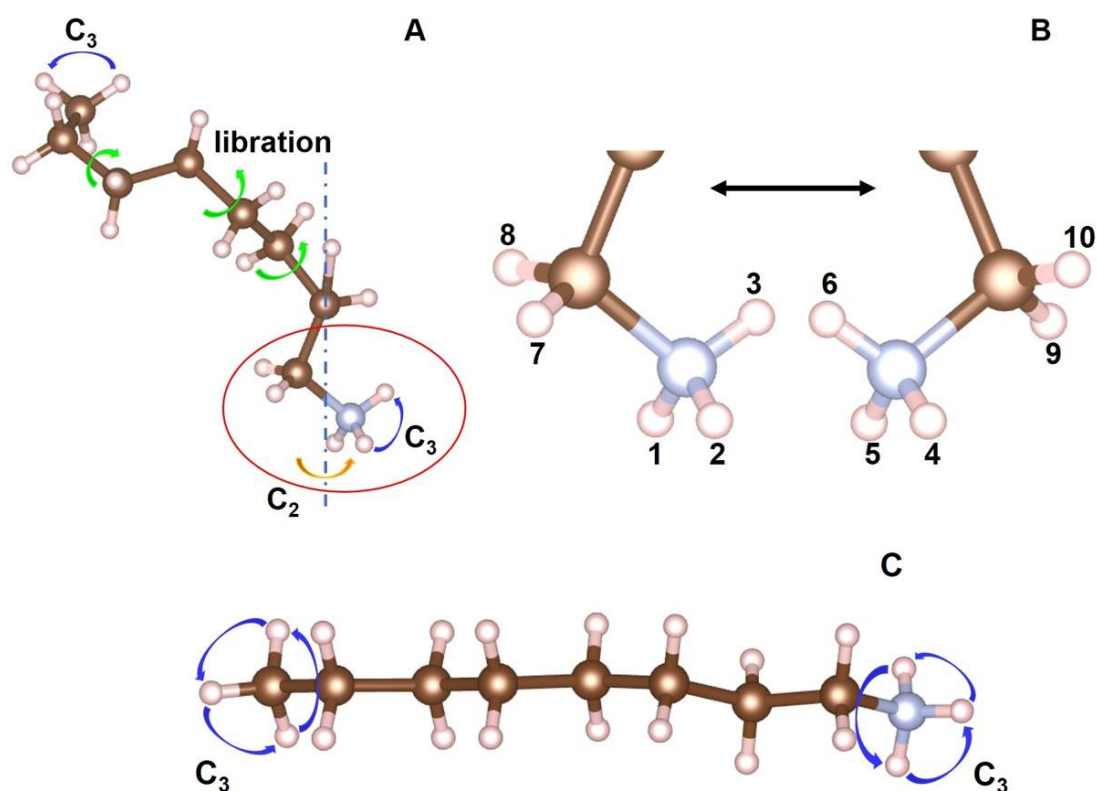


Fig. 7 Visualization of rotational modes of OA cations in different phases. (A)(B) HT phase: C₃ of CH₃, C₂ ⊗ C₃ of NH₃, C₂ of the adjacent CH₂ and slow librations of other CH₂ groups. (C) IT and LT phase: C₃ of CH₃ and NH₃.

beyond the edge of the inorganic cage in the HT phase, with the unique axis chosen to be the *c*-axis ($c > a, b$). This configuration prohibits the whole-molecular rotation around the *c*-direction due to steric hindrance from neighboring OA⁺ cations. As summarized in details in the

supplementary information, the point group of C_2 has two irreducible representations: two one-dimensional (A and B). The point group C_3 has two irreducible representations: one one-dimensional (A) and one two-dimensional (E). Thus, for the NH_3 group, $\Gamma_{NH_3} = C_2 \otimes C_3$, there are four irreducible representations: $\Gamma_{NH_3} = \{A \otimes A, A \otimes E, B \otimes A, B \otimes E\}$. For the adjacent CH_2 , $\Gamma_{CH_2} = C_2$, there two irreducible representations. For the CH_3 group at another end of molecule, $\Gamma_{CH_3} = C_3$, there are two irreducible representations. The libration behavior is modeled as a pseudo- C_2 rotation with an average jump distance $\sim 1.6 \text{ \AA}$. There are then three different relaxation times, τ_{C_2} , τ_{C_3} , and $\tau_{libration}$, that are related to the corresponding rotation operations. The fitted parameters are listed in Table. I as a function of temperature. The Q -dependence of $A_\gamma(Q)$ is obtained from the jump distance $|\mathbf{R} - C_\alpha M_\beta \mathbf{R}|$ which is calculated based upon the crystal structures. For all our analyses, the average jump distance was used in C_3 rotations of NH_3 and CH_3 groups. (see details in supplementary information).

Apart from the rotational signal, the incoherent phonons in the interested energy region cannot be ignored. Thus, we add a phonon contribution term ³⁵, which is approximated as $Q^2 e^{-\langle u^2 \rangle Q^2}$, into our neutron data fitting. The fitted U_{iso} is consistent with the refined root-mean-square cation atomic displacements (Fig. 3). Before using this combination model, we tried other models but these other models could

not reproduce the Q – dependence of the data. As shown in Fig. 5 and Fig. 6, the combination of the models presented in this section can reproduce the data decently well over $310 \text{ K} \leq T \leq 370 \text{ K}$, in the HT phase. The corresponding fitting parameters are plotted in Fig. 8 and listed in Table.

I.

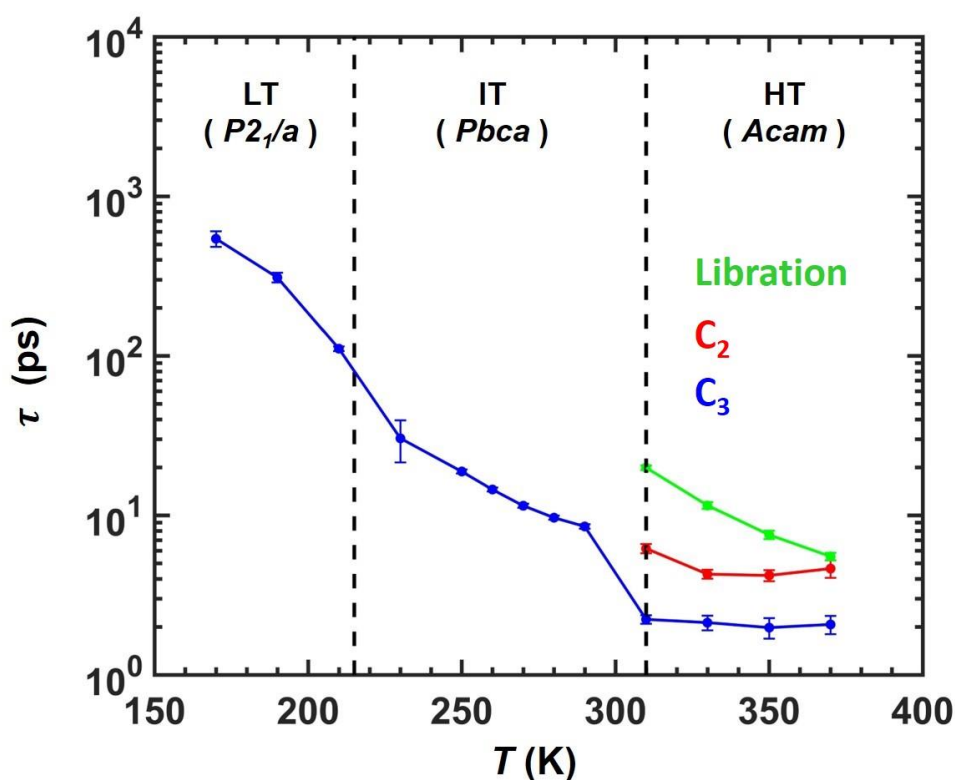


Fig. 8 Relaxation times of rotational modes of OA cations in different phases. τ_{C_2} (red), τ_{C_3} (blue) and $\tau_{libration}$ (green). Vertical black dash lines indicate the phase transition temperatures upon cooling.

Table. I Relaxation times τ_{C_2} and τ_{C_3} for the rotational modes of OA^+ cation, respectively. The values were obtained by fitting the CNCS data using the rotational model above. $\langle u^2 \rangle$ is the displacement for the Debye – Waller factor, $e^{-\langle u^2 \rangle Q^2}$. The errors in the parentheses were estimated by the least square fitting with 95%

confidence.

Phase	T (K)	τ_{c_2} (ps)	τ_{c_3} (ps)	$\tau_{libration}$ (ps)	$\langle u^2 \rangle$ (\AA^2)
HT (<i>Acam</i>)	370	4.63(7)	2.07(7)	5.52(9)	0.223(5)
	350	4.19 (3)	1.97(9)	7.54(4)	0.194(5)
	330	4.27(8)	2.12(2)	11.53(5)	0.170(4)
	310	6.19(1)	2.22(3)	19.89(7)	0.145(2)
IT (<i>Pbca</i>)	290	∞	8.51(6)	∞	0.131(2)
	280	∞	9.65(8)	∞	0.120(2)
	270	∞	11.48(3)	∞	0.113(2)
	260	∞	14.50(1)	∞	0.108(2)
	250	∞	18.81(3)	∞	0.105(2)
LT (<i>P2₁/a</i>)	230	∞	30(9)	∞	0.098(2)
	210	∞	110(4)	∞	0.075(1)
	190	∞	309(21)	∞	0.063(1)
	170	∞	542(60)	∞	0.057(1)

In the IT and LT phases, the partial-molecular rotation is abandoned mainly because of the great mis-match in Q – dependence fitting. Due to the same reason, the librations are ruled out. Only C_3 rotations of the NH_3 and CH_3 groups are applied. Details are discussed in the supplementary information.

Our results on the rotational dynamics and the structures provide us that the major difference among 350 K, 270 K and 20 K is the difference in the rotational dynamics: as shown in Fig. 5-7 and as discussed in the

text, at both 20 K and 270 K only the C_3 rotations of the two terminal CH_3 and NH_3 groups are active, and the rest part of the cation is frozen (see Fig. 7C). We believe that this is the reason for the shape of the organic cation being more or less the same for both temperatures. On the other hand, at 350 K in the high-temperature orthorhombic phase the rotational dynamics is much more complex, involving a C_2 rotation of the NH_3-CH_2 head group and librations of the other CH_2 groups in addition to the C_3 rotations of the CH_3 and NH_3 . The different rotational dynamics in the HT phase might be the reason for the bending of the organic cation in the phase.

CONCLUSION

In this paper, we have characterized the structural phase transitions and rotational dynamics of the organic cation in a two-dimensional MHP, $(OA)_2PbI_4$, as a function temperature. We have shown that the two structural phase transitions have thermal hysteresis, resulting from the existence of the potential barriers between the structural phases, and the transitions are due to the changes in the vibrational and rotational entropy. As for the rotational dynamics, our results show that in the high-temperature phase, the OA cation exhibits a combination of a two-fold rotation of the $NH_3 - CH_2$ head group around the c -axis of the

crystallographic unit cell, three-fold rotations of the NH_3 and CH_3 groups and slow librations of the other CH_2 groups, while in the intermediate-temperature and low-temperature phases, only the three-fold rotations remain. There is a consensus that excitonic features dominate in 2D MHPs while in 3D MHPs more polaronic features dominate. It remains to be seen that whether or not rotational dynamics affects the optoelectronic properties in 2D MHPs.

SUPPLEMENTARY MATERIAL

The supplementary material includes the sample preparation procedures, the refined crystal structures at different temperatures, and the detailed calculations and discussions involved in the rotational dynamic analysis.

ACKNOWLEDGEMENT

The work at the University of Virginia was supported by the U.S. Department of Energy, Office of Science, Office of Basic Energy Sciences under Award Number DE-SC0016144. The research at Oak Ridge National Laboratory's Spallation Neutron Source was sponsored by the U.S. Department of Energy, Office of Basic Energy Sciences. This research used resources at Spallation Neutron Source, a DOE Office of Science User Facility operated by the Oak Ridge National Laboratory. The computational work was performed by utilizing the resources at the National Energy Research Scientific Computing (NERSC) Center, which

is supported by the Office of Science of the U.S. Department of Energy (Contract No. DE-AC02-05CH11231). We acknowledge the support of the National Institute of Standards and Technology, U. S. Department of Commerce, in providing the neutron research facilities used in this work.

REFERENCES

- 1 M. R. Filip, G. E. Eperon, H. J. Snaith and F. Giustino. Steric engineering of metal-halide perovskites with tunable optical band gaps. *Nature Communications* **5**
- 2 S. D. Stranks and H. J. Snaith. Metal-halide perovskites for photovoltaic and light-emitting devices. *Nature Nanotechnology* **10**, 391, doi:10.1038/nnano.2015.90 (2015).
- 3 L. M. Herz. Charge-carrier mobilities in metal halide perovskites: fundamental mechanisms and limits. *ACS Energy Lett.* **2**, 1539-1548 (2017).
- 4 M. B. Johnston and L. M. Herz. Hybrid perovskites for photovoltaics: charge-carrier recombination, diffusion and radiative efficiencies. *Acc. Chem. Res.* **49**, 146-154 (2016).
- 5 Y. Chen, H. T. Yi, X. Wu, R. Haroldson, Y. N. Gartstein, Y. I. Rodionov, K. S. Tikhonov, A. Zakhidov, X. -Y. Zhu and V. Podzorov. Extended carrier lifetimes and diffusion in hybrid perovskites revealed by Hall effect and photoconductivity measurements. *Nature Communications* **7**, 12253 (2016).
- 6 T. Chen, W. -L. Chen, B. J. Foley, J. Lee, J. P. C. Ruff, J. Y. Peter Ko, C. M. Brown, L. W. Harriger, D. Zhang, C. Park, M. Yoon, Y. -M. Chang, J. J. Choi

- and S. -H. Lee. Origin of long lifetime of band-edge charge carriers in organic–inorganic lead iodide perovskites. *PNAS* **114**, 7519-7524, doi:10.1073/pnas.1704421114 (2017).
- 7 S. De Wolf, J. Holovsky, S. -J. Moon, P. Loper, B. Niesen, M. Ledinsky, F. -J Haug, J. -H. Yum and C. Ballif. Organometal halide perovskites: sharp optical absorption edge and its relation to photovoltaic performance. *J. Phys. Chem. Lett.* **5**, 1035-1039 (2014).
- 8 T.-T. Sha, Y.-A. Xiong, Q. Pan, X.-G. Chen, X.-J. Song, J. Yao, S.-R. Miao, Z.-Y. Jing, Z.-J. Feng, Y.-M. You and R.-G. Xiong. Fluorinated 2D lead iodide perovskite ferroelectrics. *Adv. Mater.* **31**, 1901843 (2019).
- 9 W.-Q. Liao, D. Zhao, Y.-Y. Tang, Y. Zhang, P.-F. Li, P.-P. Shi, X.-G. Chen, Y.-M. You and R.-G. Xiong. A molecular perovskite solid solution with piezoelectricity stronger than lead zirconate titanate. *Science* **363**, 1206-1210 (2019).
- 10 H.-Y. Ye, Y.-Y. Tang, P.-F. Li, W.-Q. Liao, J.-X. Gao, X.-N. Hua, H. Cai, P.-P. Shi, Y.-M. You and R.-G. Xiong. Metal-free three-dimensional perovskite ferroelectrics.
- 11 C.-K. Yang, W.-N. Chen, Y.-T. Ding, J. Wang, Y. Rao, W.-Q. Liao, Y.-Y. Tang, P.-F. Li, Z.-X. Wang and R.-G. Xiong. The first 2D homochiral lead iodide perovskite ferroelectrics: [*R*- and *S*-1-(4-chlorophenyl)ethylammonium]₂PbI₄. *Adv. Mater.* **31**, 1808088 (2019).

- 12 D. A. Valverde-Chavez, C. S. Ponseca Jr., C. C. Stoumpos, A. Yartsev, M. G. Kanatzidis, V. Sundstrom and D. G. Cooke. Intrinsic femtosecond charge generation dynamics in single crystal $\text{CH}_3\text{NH}_3\text{PbI}_3$. *Energy Environ. Sci* **8**, 3700-3707 (2015).
- 13 D. Cortecchia, J. Yin, A. Bruno, S. -Z. A. Lo, G. G. Gurzadyan, S. Mhaisalkar, J. -L. Bredas, C. Soci. Polaron self-localization in white-light emitting hybrid perovskites. *Journal of Materials Chemistry C* **5**, 2771-2780 (2017).
- 14 K. Miyata, D. Meggiolaro, M. T. Trinh, P. P. Joshi, E. Mosconi, S. C. Jones, F. De Angelis and X. -Y. Zhu. Large polarons in lead halide perovskites. *Science advances* **3**, e1701217 (2017).
- 15 W. S. Yang, B. -W. Park, E. H. Jung, N. J. Jeon, Y. C. Kim, D. U. Lee, S. S. Shin, J. Seo, E. K. Kim, J. H. Noh and S. II Seok.. Iodide management in formamidinium-lead-halide-based perovskite layers for efficient solar cells. *Science* **356**, 1376-1379 (2017).
- 16 A. Slonopas, B. J. Foley, J. J. Choi and M. C. Gupta. Charge transport in bulk $\text{CH}_3\text{NH}_3\text{PbI}_3$ perovskite. *J. Appl. Phys.* **119**, 074101 (2016).
- 17 T. Ivanovska, C. Dionigi, E. Mosconi, F. De Angelis, F. Liscio, V. Morandi and G. Ruani. Long-lived photoinduced polarons in organohalide perovskites. *J. Phys. Chem. Lett.* **8**, 3081-3086 (2017).

- 18 F. Zheng and L. -W. Wang. Large Polaron Formation and its Effect on Electron Transport in Hybrid Perovskite. *Energy & Environmental Science* (2019).
- 19 X. Yang, Y. Wang, H. Li and C. -X. Sheng. Optical properties of heterojunction between hybrid halide perovskite and charge transport materials: exciplex emission and large polaron. *J. Phys. Chem. C* **120**, 23299-23303 (2016)
- 20 K. Zheng, M. Abdellah, Q. Zhu, Q. Kong, G. Jennings, C. A. Kurtz, M. E. Messing, Y. Niu, D. J. Gosztola, M. J. Al-Marri, X. Zhang, T. Pullerits and S. E. Canton. Direct experimental evidence for photoinduced strong-coupling polarons in organolead halide perovskite nanoparticles. *J. Phys. Chem. Lett.* **7**, 4535-4539 (2016).
- 21 X. -Y. Zhu and V. Podzorov. Charge carriers in hybrid organic–inorganic lead halide perovskites might be protected as large polarons. *J. Phys. Chem. Lett.* **6**, 4758-4761 (2015).
- 22 P. P. Joshi, S. F. Maehrlein, X. -Y. Zhu. Dynamics screening and slow cooling of hot carriers in lead halide perovskites. *Advanced Materials*, 1803054 (2019).
- 23 K. Miyata and X. -Y. Zhu. Ferroelectric large polarons. *Nature materials* **17**, 379 (2018).

- 24 J. C. Blancon, A. V. Stier, H. Tsai, W. Nie, K. Stoumpos, B. Traore, L. Pedesseau, M. Kepenekian, F. Katsutani, G. T. Noe, J. Kono, S. Tretiak, S. A. Crooker, C. Katan, M. Kanatzidis, J. J. Crochet, J. Even and A. D. Mohite. Scaling law for excitons in 2D perovskite quantum wells. *Nature communications* **9**, 2254 (2018).
- 25 Y. Gao, M. Zhang, X. Zhang and G. Lu. Decreasing exciton binding energy in two-dimensional halide perovskites by lead vacancies. *J. Phys. Chem. Lett.* **10**, 3820-3827 (2019).
- 26 F. Thouin, D. A. Valverde-Chavez, C. Quarti, D. Cortecchia, I. Bargigia, D. Beljonne, A. Petrozza, C. Silva and A. R. S. Kandada. Phonon coherences reveal the polaronic character of excitons in two-dimensional lead halide perovskites. *Nature materials* **1** (2019).
- 27 S. Neutzner, F. Thouin, D. Cortecchia, A. Petrozza, C. Silva and A. R. S. Kandada. Exciton-polaron spectral structures in two-dimensional hybrid lead halide perovskites. *Physical Review Materials* **2**, 064605 (2018).
- 28 J. Yin, H. Li, D. Cortecchia, C. Soci and J. -L. Bredas. Excitonic and polaronic properties of 2D hybrid organic-inorganic perovskites. *ACS Energy Letters* **2**, 417-423 (2017).
- 29 N. P. Gallop, O. Selig, G. Giubertoni, H. J. Bakker, Y. L. A. Rezus, J. M. Frost, T. L. C. Jansen, R. Lovrincic and A. A. Bakulin. Rotational cation dynamics in metal halide perovskites: effect on phonons and material properties. *J. Phys. Chem. Lett.* **9**, 5987-5997 (2018).

- 30 T. Hakamata, K. Shimamura, F. Shimojo, R. K. Kalia, A. Nakano and P. Vashishta. The nature of free-carrier transport in organometal halide perovskites. *Sci. Rep.* **6**, 19599 (2016).
- 31 J. Gong, M. Yang, X. Ma, R. D. Schaller, G. Liu, L. Kong, Y. Yang, M. C. Beard, M. Lesslie, Y. Dai, B. Huang, K. Zhu and T. Xu. Electron-rotor interaction in organic-inorganic lead iodide perovskites discovered by isotope effects. *J. Phys. Chem. Lett.* **7**, 15, 2879-2887 (2016).
- 32 M. Bonn, K. Miyata, E. Hendry and X.-Y. Zhu. Role of dielectric drag in polaron mobility in lead halide perovskites. *ACS Energy Letters* **2**, 2555-2562 (2017).
- 33 T. Chen, B. J. Foley, B. Ipek, M. Tyagi, J. R. D. Copley, C. M. Brown, J. J. Choi and S. -H. Lee. Rotational dynamics of organic cations in $\text{CH}_3\text{NH}_3\text{PbI}_3$ perovskite. *Phys. Chem. Chem. Phys.*, 2015, **17**, 31278.
- 34 A. Lemmerer and D. G. Billing. Synthesis, characterization and phase transitions of the inorganic-organic layered perovskite-type hybrids $[(\text{C}_n\text{H}_{2n+1}\text{NH}_3)_2\text{PbI}_4]$, $n=7, 8, 9$ and 10 . *Dalton Trans.*, 2012, **41**, 1146.
- 35 M. Bée. *Quasielastic Neutron Scattering*. Adam Hilger, Bristol (1988).

Supplementary Online Material for Crystal Structures and Rotational Dynamics of a Two- dimensional Metal Halide Perovskite (OA)₂PbI₄

This PDF file includes:

1. Sample preparations
2. Differential Scanning Calorimetry measurements
3. Rietveld refinements results of (OA)₂PbI₄ at different temperatures
4. Quasi-elastic neutron scattering and rotational mode analysis of (OA)₂PbI₄

Supporting Online Material

1. Rietveld Refinements for the Three Structural Phases of $(OA)_2PbI_4$

All the powder samples were synthesized in the Choi Laboratory for Optoelectronic Nanomaterials of the Department of Chemical Engineering, University of Virginia.

OAI in a powder form was purchased from GreatCell Solar. Deuterated OA was purchased from CDN Isotopes. Hydriodic acid (HI, 57 wt.% in H_2O), hypophosphorous acid (H_3PO_2 , 50% aqueous), gamma butyrolactone (gBL), OA and anhydrous toluene were purchased from Sigma Aldrich. PbI_2 in a powder form was purchased from TCI America.

Deuterated $(OA)_2PbI_4$: Deuterated OAI was neutralized with HI in ice bath at molar ratio of 1:1.5. The solution is vacuum dried and washed with toluene 3 times before vacuum dried overnight. PbI_2 and deuterated OAI were dissolved in gBL at molar ratio of 2:1, and then the solution was added drop-wise into anhydrous toluene. The precipitation was collected with centrifugation and washed with toluene 3 times before dried in vacuum for 5 hours at $75^\circ C$.

$(OA)_2PbI_4$: PbI_2 and non-deuterated OAI were dissolved in gBL at molar ratio of 2:1, and then the solution was added drop-wise into anhydrous toluene. The precipitation was collected with centrifugation and washed with toluene 3 times before dried in vacuum for 5 hours at $75^\circ C$.

2. Differential Scanning Calorimetry (DSC) measurements of (OA)₂PbI₄

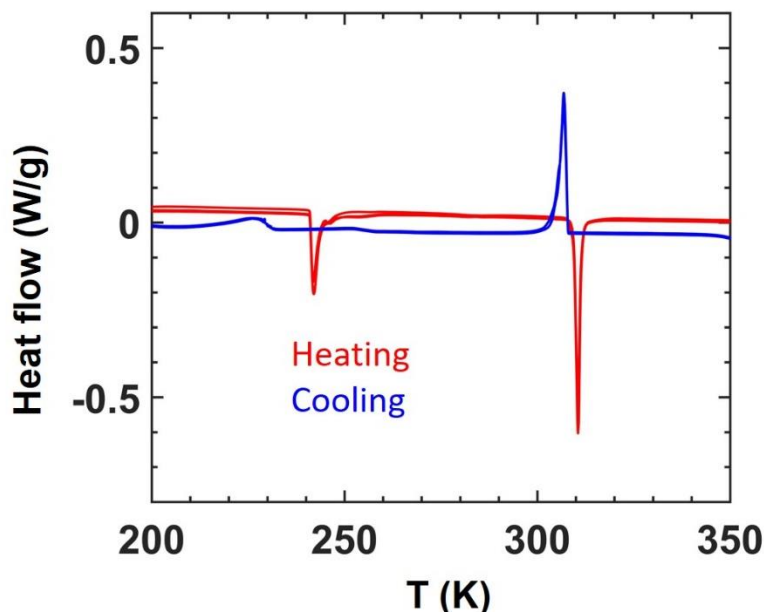


Fig. S1 Differential Scanning Calorimetry measurements of (OA)₂PbI₄. The Differential Scanning Calorimetry measurements are performed on a non-deuterated (OA)₂PbI₄ sample. Two reversible phase transitions are detected. The hysteresis and transition temperatures are consistent with our SPINS data.

3. Rietveld Refinements for the Three Structural Phases of (OA)₂PbI₄

The Bragg peaks were fitted using the Rietveld refinement method to determine the crystal structures at low temperature (LT) phase, intermediate temperature (IT) phase and high temperature (HT) phase, using GSAS (*S1*) package along with EXPGUI (graphical user interface) (*S2*). The initial structures used for Rietveld refinement were taken from a previous structure study (*S3*) based on the X-ray measurements.

Our neutron diffraction measurements, which have a higher sensitivity on the light atoms, provided more accurate organic atom positions than the X-ray results. The crystal structures were determined to be monoclinic with a $P2_1/a$ space group in LT phase, orthorhombic with a $Pbca$ space group in IT phase, and orthorhombic with an $Acam$ space group in HT phase. The crystal parameters are listed in Table. S I-S VIII.

Table. SI Crystal structural parameters of the deuterated (OA)₂PbI₄ monoclinic

($P2_1/a$ LT) phase at 20 K. The lattice parameters are $a = 8.4289 \text{ \AA}$, $b = 8.9497 \text{ \AA}$, $c = 18.5813 \text{ \AA}$, $\beta = 96.0328^\circ$. The goodness of the refinement is $\chi^2 = 7.252$.

Label	Atom	x	y	z	Occ.	U_{iso}	Site
Pb	Pb	0.00000	0.00000	0.00000	1	0.038	2a
I1	I	0.98415	0.92548	0.83496	1	0.022	4e
I2	I	0.68798	1.19851	0.96709	1	0.039	4e
N	N	0.92824	0.54348	0.86831	1	0.052	4e
H1A	H	0.96278	0.66267	0.87790	1	0.212	4e
H1B	H	1.00064	0.47142	0.90788	1	0.212	4e
H1C	H	0.79909	0.52931	0.87511	1	0.212	4e
C1	C	0.95544	0.50253	0.79798	1	0.005	4e
D1D	D	1.07828	0.47610	0.79664	1	0.068	4e
D1E	D	0.92020	0.57558	0.75286	1	0.068	4e
C2	C	0.89291	0.34552	0.77811	1	0.012	4e
D2A	D	0.76363	0.33487	0.77615	1	0.050	4e
D2B	D	0.94616	0.27596	0.82221	1	0.050	4e
C3	C	0.93459	0.28434	0.70421	1	0.017	4e
D3A	D	1.06614	0.28034	0.70259	1	0.017	4e
D3B	D	0.88843	0.17367	0.69231	1	0.017	4e
C4	C	0.85574	0.36880	0.63452	1	0.020	4e
D4A	D	0.72492	0.37226	0.63420	1	0.022	4e
D4B	D	0.89901	0.48566	0.63324	1	0.022	4e
C5	C	0.90088	0.30824	0.56331	1	0.021	4e
D5A	D	1.02829	0.31387	0.56811	1	0.026	4e
D5B	D	0.86652	0.18850	0.55970	1	0.026	4e
C6	C	0.81592	0.37151	0.49698	1	0.022	4e
D6A	D	0.85880	0.48274	0.49821	1	0.026	4e
D6B	D	0.68563	0.37575	0.49819	1	0.026	4e
C7	C	0.84812	0.29350	0.42704	1	0.022	4e

D7A	D	0.81232	0.17325	0.43332	1	0.026	4e
D7B	D	0.97572	0.29610	0.42219	1	0.026	4e
C8	C	0.78355	0.36812	0.35355	1	0.037	4e
D8A	D	0.83904	0.31578	0.30811	1	0.064	4e
D8B	D	0.81220	0.48802	0.35571	1	0.064	4e
D8C	D	0.65343	0.35395	0.34473	1	0.064	4e

Table. SII Crystal structural parameters of the deuterated (OA)₂PbI₄ monoclinic (P2₁/a LT) phase at 120 K. The lattice parameters are $a = 8.4538 \text{ \AA}$, $b = 8.9828 \text{ \AA}$, $c = 18.6716 \text{ \AA}$, $\beta = 96.3104^\circ$. The goodness of the refinement is $\chi^2 = 5.938$.

Label	Atom	x	y	z	Occ.	U _{iso}	Site
Pb	Pb	0.00000	0.00000	0.00000	1	0.025	2a
I1	I	1.00088	0.91387	0.83681	1	0.070	4e
I2	I	0.68945	1.20057	0.96864	1	0.034	4e
N	N	0.91250	0.55459	0.86574	1	0.055	4e
H1A	H	0.95016	0.67196	0.87444	1	0.126	4e
H1B	H	0.97022	0.48448	0.91028	1	0.126	4e
H1C	H	0.78102	0.54680	0.86468	1	0.126	4e
C1	C	0.95996	0.50166	0.79644	1	0.035	4e
D1D	D	1.08724	0.49565	0.79185	1	0.059	4e
D1E	D	0.90710	0.57743	0.75515	1	0.059	4e
C2	C	0.88916	0.34967	0.77599	1	0.042	4e
D2A	D	0.75763	0.34361	0.77596	1	0.060	4e
D2B	D	0.94459	0.26674	0.81676	1	0.060	4e
C3	C	0.92997	0.28611	0.70431	1	0.047	4e
D3A	D	1.05783	0.30508	0.70054	1	0.050	4e
D3B	D	0.90514	0.16994	0.69231	1	0.050	4e
C4	C	0.84713	0.36555	0.63391	1	0.050	4e

D4A	D	0.71704	0.36833	0.63493	1	0.037	4e
D4B	D	0.88959	0.48077	0.63465	1	0.037	4e
C5	C	0.90228	0.31419	0.56413	1	0.051	4e
D5A	D	1.03108	0.30538	0.56630	1	0.061	4e
D5B	D	0.85379	0.20128	0.56183	1	0.061	4e
C6	C	0.81449	0.37178	0.49889	1	0.052	4e
D6A	D	0.85324	0.48593	0.49608	1	0.057	4e
D6B	D	0.68500	0.37219	0.49710	1	0.057	4e
C7	C	0.85159	0.29704	0.42821	1	0.052	4e
D7A	D	0.81614	0.17830	0.43100	1	0.048	4e
D7B	D	0.98073	0.30073	0.42736	1	0.048	4e
C8	C	0.78068	0.36865	0.35650	1	0.061	4e
D8A	D	0.81996	0.30772	0.31053	1	0.101	4e
D8B	D	0.82006	0.48338	0.35489	1	0.101	4e
D8C	D	0.65135	0.36579	0.35319	1	0.101	4e

Table. SIII Crystal structural parameters of the deuterated (OA)₂PbI₄ monoclinic (P2₁/a LT) phase at 200 K. The lattice parameters are $a = 8.4870 \text{ \AA}$, $b = 8.9753 \text{ \AA}$, $c = 18.7542 \text{ \AA}$, $\beta = 96.5412^\circ$. The goodness of the refinement is $\chi^2 = 6.473$.

Label	Atom	x	y	z	Occ.	U _{iso}	Site
Pb	Pb	0.00000	0.00000	0.00000	1	0.035	2a
I1	I	0.99422	0.92450	0.84121	1	0.072	4e
I2	I	0.68295	1.19795	0.96742	1	0.041	4e
N	N	0.91109	0.55063	0.86530	1	0.067	4e
H1A	H	0.95681	0.66366	0.87760	1	0.160	4e
H1B	H	0.96272	0.47277	0.90695	1	0.160	4e
H1C	H	0.78099	0.55062	0.86394	1	0.160	4e
C1	C	0.95395	0.50423	0.79583	1	0.049	4e

D1D	D	1.08112	0.49506	0.79038	1	0.073	4e
D1E	D	0.90057	0.57917	0.75344	1	0.073	4e
C2	C	0.88544	0.35114	0.77389	1	0.056	4e
D2A	D	0.75701	0.33855	0.77627	1	0.072	4e
D2B	D	0.94772	0.27480	0.81376	1	0.072	4e
C3	C	0.92875	0.28953	0.70161	1	0.061	4e
D3A	D	1.05538	0.31161	0.69903	1	0.057	4e
D3B	D	0.90877	0.16975	0.69283	1	0.057	4e
C4	C	0.84772	0.36878	0.63251	1	0.064	4e
D4A	D	0.71923	0.37058	0.63544	1	0.058	4e
D4B	D	0.88909	0.48473	0.63273	1	0.058	4e
C5	C	0.89466	0.31195	0.56322	1	0.065	4e
D5A	D	1.02347	0.30078	0.56380	1	0.067	4e
D5B	D	0.84403	0.19933	0.56225	1	0.067	4e
C6	C	0.80956	0.37226	0.49923	1	0.066	4e
D6A	D	0.84323	0.48956	0.49500	1	0.059	4e
D6B	D	0.67996	0.36719	0.49645	1	0.059	4e
C7	C	0.84646	0.29497	0.42463	1	0.066	4e
D7A	D	0.82221	0.17544	0.43001	1	0.072	4e
D7B	D	0.97562	0.31187	0.42955	1	0.072	4e
C8	C	0.78053	0.36157	0.35937	1	0.076	4e
D8A	D	0.81255	0.29678	0.31311	1	0.102	4e
D8B	D	0.82577	0.47416	0.35648	1	0.102	4e
D8C	D	0.65146	0.36528	0.35778	1	0.102	4e

Table. SIV Crystal structural parameters of the deuterated (OA)₂PbI₄ orthorhombic (*Pbca* IT) phase at 255 K. The lattice parameters are $a = 8.9430 \text{ \AA}$, $b = 8.6794 \text{ \AA}$, $c = 37.5122 \text{ \AA}$. The goodness of the refinement is $\chi^2 = 1.440$.

Label	Atom	x	y	z	Occ.	U _{iso}	Site
Pb	Pb	0.00000	0.00000	0.00000	1	0.187	4a
I1	I	1.01771	0.97680	0.91595	1	0.228	8c
I2	I	0.69703	1.19427	0.99652	1	0.130	8c
N	N	1.06373	0.57838	0.93329	1	0.236	8c
H1A	H	1.06031	0.57354	0.95696	1	0.215	8c
H1B	H	1.03817	0.67261	0.92612	1	0.215	8c
H1C	H	1.15608	0.55736	0.92587	1	0.215	8c
C1	C	0.96042	0.46673	0.91831	1	0.185	8c
D1D	D	0.85833	0.49141	0.92485	1	0.481	8c
D1E	D	0.98372	0.36383	0.92667	1	0.481	8c
C2	C	0.98098	0.47820	0.87888	1	0.201	8c
D2A	D	1.08369	0.45202	0.87324	1	0.247	8c
D2B	D	0.96508	0.58427	0.87173	1	0.247	8c
C3	C	0.87825	0.37537	0.85643	1	0.209	8c
D3A	D	0.90446	0.26792	0.85937	1	0.314	8c
D3B	D	0.77463	0.38976	0.86343	1	0.314	8c
C4	C	0.90280	0.42628	0.81808	1	0.229	8c
D4A	D	0.85617	0.52683	0.81521	1	0.294	8c
D4B	D	1.00898	0.43977	0.81444	1	0.294	8c
C5	C	0.84446	0.32336	0.78905	1	0.240	8c
D5A	D	0.73666	0.31536	0.79060	1	0.211	8c
D5B	D	0.88699	0.22120	0.79141	1	0.211	8c
C6	C	0.88972	0.39294	0.75315	1	0.254	8c
D6A	D	0.85064	0.49726	0.75179	1	0.271	8c
D6B	D	0.99755	0.39922	0.75209	1	0.271	8c
C7	C	0.83431	0.30445	0.72135	1	0.266	8c
D7A	D	0.72620	0.29785	0.72231	1	0.405	8c
D7B	D	0.87370	0.20007	0.72241	1	0.405	8c

C8	C	0.88126	0.37813	0.68646	1	0.226	8c
D8A	D	0.85279	0.31279	0.66701	1	0.297	8c
D8B	D	0.98799	0.39201	0.68632	1	0.297	8c
D8C	D	0.83329	0.47644	0.68409	1	0.297	8c

Table. SV Crystal structural parameters of the deuterated (OA)₂PbI₄ orthorhombic (*Pbca* IT) phase at 270 K. The lattice parameters are $a = 8.9660 \text{ \AA}$, $b = 8.6873 \text{ \AA}$, $c = 37.5264 \text{ \AA}$. The goodness of the refinement is $\chi^2 = 5.891$.

Label	Atom	x	y	z	Occ.	U _{iso}	Site
Pb	Pb	0.00000	0.00000	0.00000	1	0.031	4a
I1	I	1.00802	0.98024	0.91475	1	0.054	8c
I2	I	0.69539	1.19244	0.99905	1	0.237	8c
N	N	1.06031	0.57241	0.93685	1	0.086	8c
H1A	H	1.05485	0.56863	0.96050	1	0.097	8c
H1B	H	1.03941	0.66734	0.92939	1	0.097	8c
H1C	H	1.15201	0.54700	0.92989	1	0.097	8c
C1	C	0.95383	0.46505	0.92161	1	0.228	8c
D1D	D	0.85264	0.49452	0.92763	1	0.454	8c
D1E	D	0.97202	0.36161	0.93026	1	0.454	8c
C2	C	0.97788	0.47408	0.88227	1	0.244	8c
D2A	D	1.07955	0.44312	0.87716	1	0.307	8c
D2B	D	0.96711	0.58039	0.87486	1	0.307	8c
C3	C	0.87294	0.37520	0.85956	1	0.252	8c
D3A	D	0.89426	0.26689	0.86282	1	0.349	8c
D3B	D	0.76976	0.39449	0.86606	1	0.349	8c
C4	C	0.90256	0.42346	0.82125	1	0.272	8c
D4A	D	0.86060	0.52580	0.81799	1	0.164	8c
D4B	D	1.00921	0.43201	0.81807	1	0.164	8c

C5	C	0.84235	0.32226	0.79216	1	0.282	8c
D5A	D	0.73449	0.31917	0.79324	1	0.180	8c
D5B	D	0.88020	0.21846	0.79490	1	0.180	8c
C6	C	0.89321	0.38830	0.75636	1	0.296	8c
D6A	D	0.85881	0.49412	0.75463	1	0.301	8c
D6B	D	1.00099	0.38968	0.75578	1	0.301	8c
C7	C	0.83675	0.30126	0.72449	1	0.308	8c
D7A	D	0.72868	0.29957	0.72497	1	0.429	8c
D7B	D	0.87147	0.19535	0.72592	1	0.429	8c
C8	C	0.88938	0.37137	0.68970	1	0.523	8c
D8A	D	0.85977	0.30669	0.67026	1	0.216	8c
D8B	D	0.99632	0.38042	0.69002	1	0.216	8c
D8C	D	0.84594	0.47156	0.68693	1	0.216	8c

Table. SVI Crystal structural parameters of the deuterated (OA)₂PbI₄ orthorhombic (*Pbca* IT) phase at 285 K. The lattice parameters are $a = 8.9769 \text{ \AA}$, $b = 8.6934 \text{ \AA}$, $c = 37.4911 \text{ \AA}$. The goodness of the refinement is $\chi^2 = 1.398$.

Label	Atom	x	y	z	Occ.	U _{iso}	Site
Pb	Pb	0.00000	0.00000	0.00000	1	0.232	4a
I1	I	1.00883	0.97669	0.91595	1	0.356	8c
I2	I	0.69940	1.19665	0.99793	1	0.156	8c
N	N	1.06289	0.57673	0.93428	1	0.292	8c
H1A	H	1.05804	0.57284	0.95795	1	0.256	8c
H1B	H	1.04153	0.67155	0.92686	1	0.256	8c
H1C	H	1.15437	0.55165	0.92717	1	0.256	8c
C1	C	0.95647	0.46915	0.91916	1	0.190	8c
D1D	D	0.85547	0.49825	0.92534	1	0.523	8c
D1E	D	0.97518	0.36581	0.92777	1	0.523	8c
C2	C	0.97946	0.47839	0.87975	1	0.206	8c

D2A	D	1.08097	0.44780	0.87447	1	0.279	8c
D2B	D	0.96819	0.58462	0.87237	1	0.279	8c
C3	C	0.87437	0.37933	0.85715	1	0.214	8c
D3A	D	0.89608	0.27115	0.86036	1	0.424	8c
D3B	D	0.77142	0.39825	0.86381	1	0.424	8c
C4	C	0.90284	0.42779	0.81877	1	0.234	8c
D4A	D	0.86052	0.52994	0.81559	1	0.279	8c
D4B	D	1.00924	0.43669	0.81544	1	0.279	8c
C5	C	0.84226	0.32657	0.78972	1	0.244	8c
D5A	D	0.73457	0.32313	0.79096	1	0.252	8c
D5B	D	0.88045	0.22296	0.79239	1	0.252	8c
C6	C	0.89194	0.39286	0.75383	1	0.258	8c
D6A	D	0.85722	0.49850	0.75217	1	0.290	8c
D6B	D	0.99957	0.39459	0.75309	1	0.290	8c
C7	C	0.83500	0.30581	0.72199	1	0.270	8c
D7A	D	0.72709	0.30377	0.72263	1	0.446	8c
D7B	D	0.87004	0.20009	0.72335	1	0.446	8c
C8	C	0.88647	0.37617	0.68711	1	0.235	8c
D8A	D	0.85660	0.31151	0.66768	1	0.307	8c
D8B	D	0.99326	0.38556	0.68727	1	0.307	8c
D8C	D	0.84271	0.47615	0.68442	1	0.307	8c

Table. SVII Crystal structural parameters of the deuterated (OA)₂PbI₄ orthorhombic (*Acam* HT) phase at 325 K. The lattice parameters are $a = 8.7459 \text{ \AA}$, $b = 8.7556 \text{ \AA}$, $c = 40.7265 \text{ \AA}$. The goodness of the refinement is $\chi^2 = 1.112$.

Label	Atom	x	y	z	Occ.	U _{iso}	Site
Pb	Pb	0.00000	0.00000	0.00000	1	0.010	4a
I1	I	0.00000	0.00000	0.92402	1	0.073	8d
I2	I	0.69593	1.22185	0.00000	1	0.099	8f

N	N	1.09350	0.56265	0.94676	0.5	0.196	16g
H1A	H	1.16372	0.51857	0.95943	0.5	0.286	16g
H1B	H	1.01188	0.58592	0.95874	0.5	0.286	16g
H1C	H	1.13221	0.64725	0.93790	0.5	0.286	16g
C1	C	1.04933	0.45792	0.92076	0.5	0.327	16g
D1D	D	0.95784	0.40355	0.92725	0.5	0.311	16g
D1E	D	1.13028	0.38329	0.91755	0.5	0.311	16g
C2	C	1.02040	0.54278	0.88886	0.5	0.347	16g
D2A	D	0.91149	0.56007	0.88653	0.5	0.180	16g
D2B	D	1.07032	0.64130	0.88985	0.5	0.180	16g
C3	C	1.07777	0.45699	0.85868	0.5	0.373	16g
D3A	D	1.14534	0.37579	0.86576	0.5	0.369	16g
D3B	D	1.13670	0.52683	0.84521	0.5	0.369	16g
C4	C	0.95037	0.38903	0.83808	0.5	0.400	16g
D4A	D	0.88142	0.33249	0.85235	0.5	0.800	16g
D4B	D	0.89167	0.47158	0.82823	0.5	0.800	16g
C5	C	1.00707	0.28397	0.81108	0.5	0.410	16g
D5A	D	1.11779	0.28512	0.81102	0.5	0.800	16g
D5B	D	0.97228	0.32259	0.79010	0.5	0.800	16g
C6	C	0.95290	0.11995	0.81496	0.5	0.420	16g
D6A	D	0.97270	0.08649	0.83728	0.5	0.588	16g
D6B	D	0.84291	0.11643	0.81147	0.5	0.588	16g
C7	C	1.02910	0.00957	0.79140	0.5	0.427	16g
D7A	D	0.96782	0.00261	0.77146	0.5	0.646	16g
D7B	D	1.03232	-0.09102	0.80123	0.5	0.646	16g
C8	C	1.19046	0.05605	0.78222	0.5	0.745	16g
D8A	D	1.23230	-0.01602	0.76671	0.5	0.800	16g
D8B	D	1.25339	0.05996	0.80131	0.5	0.800	16g
D8C	D	1.18856	0.15596	0.77190	0.5	0.800	16g

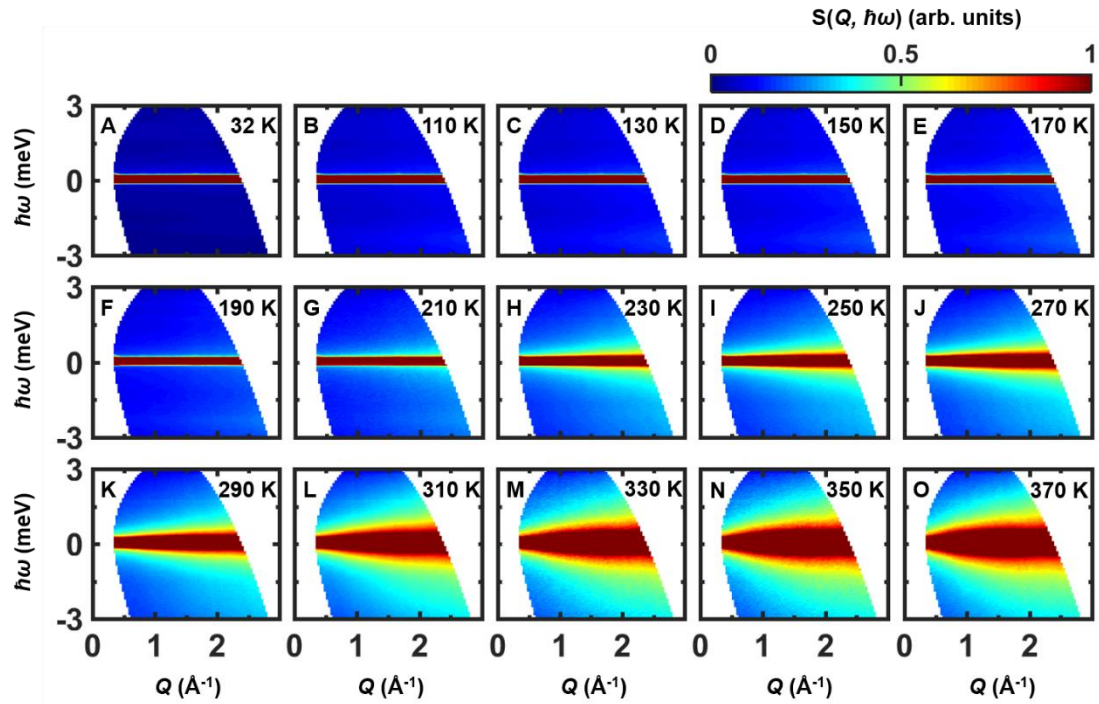
Table. SVIII Crystal structural parameters of the deuterated (OA)₂PbI₄ orthorhombic (*Acam* HT) phase at 350 K. The lattice parameters are $a = 8.7615 \text{ \AA}$, $b = 8.7634 \text{ \AA}$, $c = 41.0560 \text{ \AA}$. The goodness of the refinement is $\chi^2 = 2.415$.

Label	Atom	x	y	z	Occ.	U _{iso}	Site
Pb	Pb	0.00000	0.00000	0.00000	1	0.098	4a
I1	I	0.00000	0.00000	0.92416	1	0.154	8d
I2	I	0.73943	1.23558	0.00000	1	0.128	8f
N	N	1.07883	0.58661	0.94602	0.5	0.251	16g
H1A	H	1.15537	0.54772	0.95761	0.5	0.229	16g
H1B	H	0.99971	0.60461	0.95900	0.5	0.229	16g
H1C	H	1.10895	0.67333	0.93671	0.5	0.229	16g
C1	C	1.03428	0.47860	0.92091	0.5	0.484	16g
D1D	D	0.94895	0.41840	0.92860	0.5	0.401	16g
D1E	D	1.11882	0.40958	0.91664	0.5	0.401	16g
C2	C	0.99029	0.56045	0.88971	0.5	0.504	16g
D2A	D	0.88019	0.57030	0.88889	0.5	0.282	16g
D2B	D	1.03354	0.66204	0.88999	0.5	0.282	16g
C3	C	1.04413	0.47805	0.85907	0.5	0.530	16g
D3A	D	1.11889	0.40183	0.86517	0.5	0.581	16g
D3B	D	1.09397	0.55130	0.84491	0.5	0.581	16g
C4	C	0.91598	0.40122	0.84043	0.5	0.557	16g
D4A	D	0.85552	0.34056	0.85551	0.5	0.617	16g
D4B	D	0.84913	0.47930	0.83147	0.5	0.617	16g
C5	C	0.97140	0.29964	0.81295	0.5	0.567	16g
D5A	D	1.08135	0.30823	0.81138	0.5	0.800	16g
D5B	D	0.92797	0.33527	0.79265	0.5	0.800	16g
C6	C	0.92981	0.13259	0.81757	0.5	0.577	16g

D6A	D	0.95840	0.10111	0.83940	0.5	0.769	16g
D6B	D	0.81970	0.12159	0.81561	0.5	0.769	16g
C7	C	1.00600	0.02710	0.79322	0.5	0.584	16g
D7A	D	0.93963	0.01554	0.77432	0.5	0.634	16g
D7B	D	1.01892	-0.07271	0.80293	0.5	0.634	16g
C8	C	1.16050	0.08407	0.78192	0.5	0.800	16g
D8A	D	1.20233	0.01466	0.76601	0.5	0.800	16g
D8B	D	1.22845	0.09267	0.79996	0.5	0.800	16g
D8C	D	1.14878	0.18328	0.77171	0.5	0.800	16g

4. Quasi-elastic Neutron Scattering and Rotational Mode Analysis of $(\text{OA})_2\text{PbI}_4$

Fig. S2 Quasi-elastic neutron scattering (QENS) spectra of $(\text{OA})_2\text{PbI}_4$. (A-O) show the contour maps of QENS intensity $S(Q, \hbar\omega)$ obtained for $(\text{OA})_2\text{PbI}_4$ as a function of momentum transfer Q and energy transfer $\hbar\omega$, measured upon heating at several different temperatures spanning the three phases (LT (A-H), IT (I-K), HT (L-O)).



(This section is in the main text but is repeated here for reader convenience.)

The rotation model that accounts for the preferential molecular orientation is called jump model. In group theory, the static and dynamic structure factor for rotational motions of molecules in a crystal can be written as(S4)

$$S(Q, \hbar\omega) = e^{-\langle u^2 \rangle Q^2} \left(\sum_{\gamma} A_{\gamma}(Q) \frac{1}{\pi} \frac{\omega_{\gamma}}{1 + \omega^2 \tau_{\gamma}^2} \right) \quad (1)$$

Where the sum over γ runs over all the irreducible representations of the system group Γ , Γ_{γ} . For a polycrystalline sample, $A_{\gamma}(Q)$ is given by

$$A_{\gamma}(Q) = \frac{l_{\gamma}}{g} \sum_{\alpha} \sum_{\beta} \chi_{\gamma}^{\alpha\beta} \sum_{C_{\alpha}} \sum_{M_{\beta}} j_0(Q|R - C_{\alpha}M_{\beta}R|) \quad (2)$$

Here g is the order of group Γ and l_{γ} is the dimensionality of Γ_{γ} . The sums over α and β run over all the classes of C and M , respectively, and the sums over C_{α} and M_{β} run over all the rotations that belong to the crystal class, α , and to the molecule class, β , respectively. The characters of Γ_{γ} , $\chi_{\gamma}^{\alpha\beta}$, are the products of the characters of $C_{\gamma C}$ and $M_{\gamma M}$; $\chi_{\gamma}^{\alpha\beta} = \chi_{\gamma C}^{\alpha} \chi_{\gamma M}^{\beta}$. $j_0(x)$ is the zeroth spherical Bessel function and, $|R - C_{\alpha}M_{\beta}R|$, is the distance between the initial atom position R and final atom position $C_{\alpha}M_{\beta}R$, called the jump distance. The relaxation time for the Γ_{γ} mode, τ_{γ} , is written as

$$\frac{1}{\tau_{\gamma}} = \sum_{\alpha} \frac{n_{\alpha}}{\tau_{\alpha}} \left(1 - \frac{\chi_{\gamma}^{\alpha e}}{\chi_{\gamma}^{Ee}} \right) + \sum_{\beta} \frac{n_{\beta}}{\tau_{\beta}} \left(1 - \frac{\chi_{\gamma}^{E\beta}}{\chi_{\gamma}^{Ee}} \right) \quad (3)$$

where n_{α} , n_{β} are the number of symmetry rotations of the classes, α and β , respectively. E and e represent the identity operations of C and M .

$\Gamma = C_2 \otimes C_3$ jump model

In this model, the local crystal environment has a two-fold symmetry and the rotating part itself has a three-fold rotational symmetry. The character tables for the irreducible

representations of the C_2 and C_3 point groups are shown in Table S9.

Table. S IX Character table for $C_2 \otimes C_3$.

$C_2 \otimes C_3$	E	$2C_3$	C_2	$2C_2C_3$	$\frac{1}{\tau}$
$A \otimes A$	+1	+1	+1	+1	0
$A \otimes E$	+2	-1	+2	-1	$\frac{3}{\tau_{C_3}}$
$B \otimes A$	+1	+1	-1	-1	$\frac{2}{\tau_{C_2}}$
$B \otimes E$	+2	-1	-2	+1	$\frac{3}{\tau_{C_3}} + \frac{2}{\tau_{C_2}}$

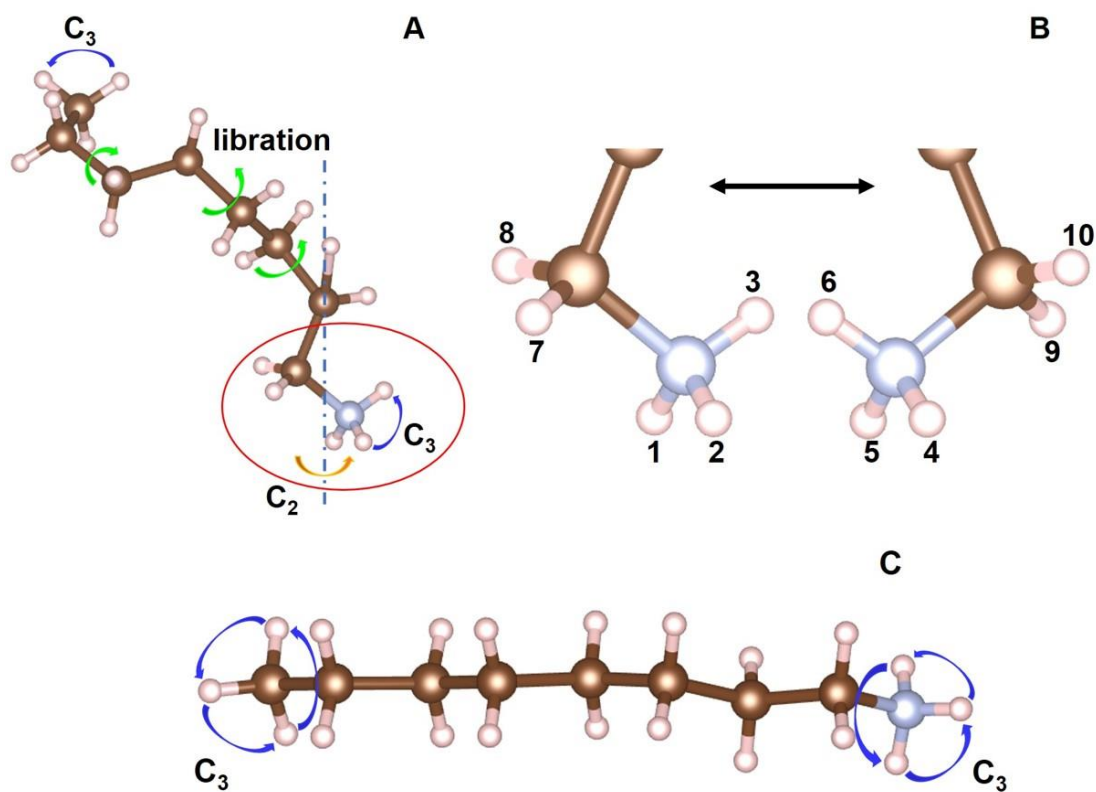


Fig. S3 (A) Visualization of rotation modes in HT phase. (B) Schematic of the CH_2 -

NH₃ terminal group (red circle part) in its C₂ rotation around *c*-axis (blue dash line) and corresponding numbered equivalent sites. Here brown balls are carbon atoms, grey balls are nitrogen atoms, and white balls are hydrogen atoms. The sites are numbered for jump distance calculation. (C) Visualization of C₃ rotations of NH₃ and CH₃ groups in IT and LT phases.

Table. S X Geometrical information for a hydrogen atom (of NH₃ group) moving from one site to another equivalent site under the combined symmetry operations of the two point groups of $\mathbf{C} = \mathbf{C}_2$ and $\mathbf{M} = \mathbf{C}_3$. The resulting jump distances r_i are, using notation $R_{i,j} = |\mathbf{R}_i - \mathbf{R}_j|$, $r = R_{1,2}$, $r_1 = R_{1,4}$, $r_2 = R_{2,5}$, $r_3 = R_{3,6}$, $r_4 = R_{1,5}$, $r_5 = R_{1,6}$, $r_6 = R_{2,6}$ where \mathbf{R}_i is the position of the *i*th hydrogen atom numbered as in Fig. S2.

Initial Position		Final Position			Jump Distance		
		E	C_3	C_3^2	E	C_3	C_3^2
1	E	1	2	3	0	r	r
	C_2	4	5	6	r_1	r_4	r_5
2	E	2	3	1	0	r	r
	C_2	5	6	4	r_2	r_6	r_4
3	E	3	1	2	0	r	r
	C_2	6	4	5	r_3	r_5	r_6

We now calculate $A_\gamma(Q)$:

$$A_{A \otimes A}(Q) = \frac{1}{18} [3 + 6j_0(Qr) + j_0(Qr_1) + j_0(Qr_2) + j_0(Qr_3) + 2j_0(Qr_4) + 2j_0(Qr_5) + 2j_0(Qr_6)]$$

$$A_{A \otimes E}(Q) = \frac{1}{18} [6 - 6j_0(Qr) + 2j_0(Qr_1) + 2j_0(Qr_2) + 2j_0(Qr_3) - 2j_0(Qr_4) - 2j_0(Qr_5) - 2j_0(Qr_6)]$$

$$A_{A \otimes A}(Q) = \frac{1}{18} [3 + 6j_0(Qr) - j_0(Qr_1) - j_0(Qr_2) - j_0(Qr_3) - 2j_0(Qr_4) - 2j_0(Qr_5) - 2j_0(Qr_6)]$$

$$A_{A \otimes A}(Q) = \frac{1}{18} [6 - 6j_0(Qr) - 2j_0(Qr_1) - 2j_0(Qr_2) - 2j_0(Qr_3) + 2j_0(Qr_4) + 2j_0(Qr_5) + 2j_0(Qr_6)]$$

where $j_0(Qr_i)$ is the zeroth spherical Bessel function.

$\Gamma = C_2 \otimes E = C_2$ jump model

Here we only consider the C_2 rotation of the hydrogen atoms on the adjacent CH_2 group from NH_3 terminal group. Based on discussion above, it is easy to calculate the correlation times τ_γ are calculated:

$$\frac{1}{\tau_A} = 0, \frac{1}{\tau_B} = \frac{2}{\tau_{C_2}}$$

The elastic and quasi-elastic incoherent structure factors $A_\gamma(Q)$ can be obtained:

$$A_A(Q) = \frac{1}{4} [2 + j_0(Qd_1) + j_0(Qd_2)]$$

$$A_B(Q) = \frac{1}{4} [2 - j_0(Qd_1) - j_0(Qd_2)]$$

where $d_1 = R_{7,9}, d_2 = R_{8,10}$ are jump distances of two hydrogen atoms on CH_2 group (shown in Fig. S2) and here we add them up to get average results in calculation since the two hydrogen atoms are equivalent.

Libration model

The libration behavior is modeled as a pseudo- C_2 rotation with an average jump distance $\sim 1.6 \text{ \AA}$. It is noted that the libration model describes not the rotation of hydrogen atoms around the carbon atoms but the deformation of the cation body consisting of the six CH_2 groups. The calculations of the relaxation time and the structure factors are similar to that in C_2 rotation:

$$\frac{1}{\tau_A} = 0, \frac{1}{\tau_B} = \frac{2}{\tau_{\text{libration}}}$$

$$A_A(Q) = \frac{1}{24} [12 + 12j_0(Qd)]$$

$$A_B(Q) = \frac{1}{24} [12 - 12j_0(Qd)]$$

where d is the average jump distance in the libration of the 6 CH₂ groups.

$\Gamma = E \otimes C_3 = C_3$ jump model

In this model, the orientation of CH₃ and NH₃ groups are fixed due to hydrogen bonding to iodide atoms. The correlation times are calculated:

$$\frac{1}{\tau_A} = 0, \frac{1}{\tau_E} = \frac{3}{\tau_{C_3}}$$

The elastic and quasi-elastic incoherent structure factors can be obtained:

$$A_A(Q) = \frac{1}{9} [3 + 6j_0(Qr)]$$

$$A_E(Q) = \frac{1}{9} [6 - 6j_0(Qr)]$$

where r is the jump distance in C_3 rotation of NH₃ and CH₃ groups.

We can fit the quasi-elastic neutron scattering data shown in Fig. S1 using the combined function ($S4$):

$$S_{fit}(Q, \hbar\omega) = A_{rot} e^{-\langle u^2 \rangle Q^2} \left(\sum_{\gamma} A_{\gamma}(Q) \frac{1}{\pi} \frac{\omega_{\gamma}}{1 + \omega^2 \tau_{\gamma}^2} \right) + A_{vib} Q^2 e^{-\langle u^2 \rangle Q^2}$$

where the first part is the rotational contribution and the second part is the vibrational contribution with the scaling factors A_{rot} and A_{vib} , respectively.

C₃ jump distances in CH₃ and NH₃ groups

Based on the refinement of the neutron diffraction data, the average C₃ jump distance of CH₃ is $r_c = 1.568$ Å and that of NH₃ is $r_n = 1.454$ Å. In all our calculations, we used the average jump distance $\bar{r} = \frac{r_c + r_n}{2}$. Then r_c and r_n can be written as $r_c = \bar{r} + \Delta$, $r_n = \bar{r} - \Delta$, where $\frac{\Delta}{\bar{r}} \approx 3.8\%$. The Q -dependence of $S(Q, \hbar\omega)$ has a functional form of the l th spherical Bessel function, $j_l(Qr)$. The difference between using two separate jump distances, r_c and r_n , and using the average jump distance, \bar{r} , is minimal:

$$j_l(Q\bar{r}) - \frac{j_l(Q(\bar{r} + \Delta)) - j_l(Q(\bar{r} - \Delta))}{2} \approx \frac{1}{2} j_l''(Q\bar{r}) Q^2 \Delta^2$$

Since $\left(\frac{\Delta}{\bar{r}}\right)^2 \approx 0.1\%$, the effect of the difference is negligible within the experimental

uncertainty.

In order to fit the data decently well, we did some modifications on the calculated jump distances to balance the influences from the structure change, the thermal fluctuation and the possible discrepancy between the calculated and real jump distances. Since we didn't perform neutron diffraction measurement at each temperature, for simplicity, we use the same set of jump distances in data fitting in the same phase.

To filter the rotational modes, we first focus on the structure configurations. For HT phase ($T > 310$ K), in principle, the OA^+ cation is much longer than MA (CH_3NH_3^+), it would be more difficult for OA^+ cation to have a whole-molecular rotation like MA ($S5$). Meanwhile, the whole-molecular rotation of OA^+ will lead to collisions between adjacent OA^+ cations indicated by its HT structure configuration. Besides the configuration, the next factor we need to consider is the Q – dependence fitting, influenced by the jump distances. We tested many other rotational models, such as C_3 rotation only of NH_3 or CH_3 groups, C_4 rotation of the $\text{NH}_3 - \text{CH}_2$ head group. They failed in the data fitting due to their great mis-match in Q . Our model is the relatively simple and energy-favorable one. Because of the similarity in jump distances of CH_3 and NH_3 groups, we cannot distinguish their C_3 rotations respectively.

As temperature is lowered, the HT-to-IT structural phase change in $(\text{OA})_2\text{PbI}_4$ occurs through a great deformation of the OA^+ cations and a slight contraction of the unit cell. This transition leads to an abrupt change in the interaction between OA^+ cations and the lead iodide octahedron. Our data shows that below the HT – IT transition temperature, the C_2 partial rotation (Fig. S3 A and B) is hard to detect and C_3 rotation still exists (Fig. S3 C). This disappearance of the partial rotation mode is in qualitative agreement with the sudden jump (main text Fig. 6 B) in the intensity of the QENS data and quantitative agreement with the mis-match in the Q – dependence of data fitting. Due to the same reason, other rotational modes such as whole-cation rotation and librations of CH_2 groups are abandoned. As temperature further goes down into LT phase, the C_3 rotation is hard to detect with an energy resolution uncovering the possible QENS signal energy window.

References

- S1 A. C. Larson and R. B. Von Dreele, Los Alamos National Laboratory, pp.86-748 (1994).
- S2 B. H. Toby, *J. Appl. Crystallogr.* **34**, 210-213 (2001).
- S3 A. Lemmerer *et al.*, "Synthesis, characterization and phase transitions in the inorganic-organic layered perovskite-type hybrids $[(C_nH_{2n+1}NH_3)_2PbI_4]$, $n = 7, 8, 9$ and 10 " *Dalton Trans.* **41**, 1146 (2007).
- S4 M. Bee', *Quasielastic Neutron Scattering* Adam, Hilger, Bristol, (1988).
- S5 Chen. T et al. Rotational dynamics of organic cations in $CH_3NH_3PbI_3$ perovskite. *Phys. Chem. Chem. Phys.*, **17**, 31278, (2015).
- S6 Certain commercial equipment, instruments, or materials are identified in this paper to foster understanding. Such identification does not imply recommendation or endorsement by the National Institute of Standards and Technology and the Oak Ridge National Laboratory, nor does it imply that the materials or equipment identified are necessarily the best available for the purpose.